Solid-state synthesis, dewetting, and magnetic and structural characterization of interfacial $Fe_xSn_{1−x}$ layers in Sn/Fe(001) thin films

V. G. Myagkov[1,a)] , V. S. Zhigalov[1], L. E. Bykova[1], L. A. Solovyov[2], A. A. Matsynin[1], Yu. Yu. Balashov[1], I. V. Nemtsev[1,3], A. V. Shabanov[1], G. N. Bondarenko[2]

[1] Kirensky Institute of Physics, Federal Research Center KSC SB RAS, Akademgorodok 50/38, Krasnoyarsk 660036, Russian Federation
[2] Institute of Chemistry and Chemical Technology, Federal Research Center KSC SB RAS, 50/24 Akademgorodok, Krasnoyarsk 660036, Russian Federation
[3] Federal Research Center Krasnoyarsk Science Center, Siberian Branch of the Russian Academy of Sciences, Akademgorodok 50, Krasnoyarsk 660036, Russian Federation
a) Address all correspondence to this author. e-mail: miagkov@iph.krasn.ru

The phase formation sequences in 9Sn/91Fe(001) and 25Sn/75Fe(001) bilayers during thin-film solid-state reactions up to 800°C were investigated using X-ray diffraction, the torque method, and scanning electron microscopy. In both samples, $FeSn_2$, FeSn, α-$Fe_{1−x}Sn_x$, Fe_5Sn_3, α-Fe, and β-Sn were sequentially formed at the initiation temperatures $T_{in}^i \sim 150°C$, $\sim 300°C$, $\sim 550°C$, $\sim 600°C$, and $\sim 700°C$, respectively. Low-temperature transformations were predicted at temperatures $T_K^1 \sim 150°C$ and $T_K^2 \sim 300°C$, which are absent in the phase equilibrium diagram of the Fe–Sn system. Solid-state dewetting of the 9Sn/91Fe(001) and 25Sn/75Fe(001) bilayers started at temperatures above 550°C. Overall, this work sheds new light on general chemical mechanisms governing the synthesis of intermetallic phases in Sn/Fe(001) thin films, the phase transformations, and the evolution of the dewetting process of $Fe_xSn_{1−x}$ films.

Introduction

In recent years, research into Fe-rich ferromagnetic compounds Fe_3Sn, Fe_5Sn_3, which have a hexagonal and Fe_3Sn_2 rhombohedral structure, has aroused great interest due to a rich variety of attractive properties for their fundamental physics and great potential applications. Fe_3Sn was studied as a potential non-rare-earth-based permanent magnet with a first magetocrystalline anisotropy constant $K_1 = 1.8$ MJ/m³. However, its c-axis is a hard magnetic axis and the magnetic easy axis lies in the basal plane, which is not very desirable for practical applications [1–3]. The crystal structure of Fe_3Sn, Fe_3Sn_2, and FeSn can be viewed as layer packaging containing the Fe_3Sn and Sn kagome planes, which generate magnetic frustrations and could result in a giant topological Hall effect [4] and a large anomalous Hall effect [5] in Fe_3Sn_2. A large topological Hall effect [6] and a large anomalous Hall effect [7] were discovered in the non-collinear magnet Fe_5Sn_3. In addition to the above, the Fe–Sn phase diagram reveals that samples with $x > 8$ at.% Sn form the solid solution α-$Fe_{1−x}Sn_x$, in which the lattice parameter expands linearly with

increasing Sn concentration according to Vegard's law [3]. A literature review showed that the structural and magnetic properties of some phases are refined [1, 8–10]. According to the phase diagram of the binary Fe–Sn system, the non-ferromagnetic $FeSn_2$ and FeSn are stable compounds at room temperature up to 773 K. The use of $FeSn_2$ as electrodes for lithium-ion batteries and FeSn as counter electrodes in photovoltaic devices has been investigated by various researchers [11–14].

Numerous studies on thin-film solid-state reactions showed the formation of only one phase, which is called the first phase, with an increase in the annealing temperature at the film interface up to a certain temperature T_{in} (known as the initiation temperature) [15–19]. With further increase in the annealing temperature, other phases could arise to form the phase sequence. Most solid-state reactions in nanofilms take place at low (100°C–400°C), room, and even cryogenic temperatures, at which diffusion is extremely low and cannot explain the atomic transfer during the reactions [20–24]. At these temperatures, the diffusion coefficient is extremely small ($D \ll 10^{-25}$ cm²/s).

Taking into account the characteristic scale of film reagents, $d \sim 100$ nm, it is easy to estimate the reaction time using the Einstein formula $t \sim d^2/D = 10^{15}$ s $\sim 10^7$ years. However, experimental data show that most solid-state reactions take 10–30 min (perhaps faster). Therefore, for low-temperature solid-state reactions to occur, the diffusion coefficient must be more than 12–18 order of magnitude higher. Low values of the diffusion coefficient, the threshold nature of the reaction, the formation of the first phase, as well as the migration of only one element (the dominant diffusing species) form the basis of our assumption that long-range chemical interactions, and not diffusion, are the main driving force in nanoscale solid-state reactions [20–24]. It is important to note that the solid-state reactions arise from long-range chemical interactions between the reacting films, separated by chemically inert barrier layers more than 2 microns thick, which are 10^4 times longer than the length of a conventional chemical bond [20–24]. Moreover, the first phase initiation temperatures T_{in} remain extremely low even as the barrier layer thickness is increased to 2 microns.

Our previous studies and analysis of solid-state reactions for many bilayer films showed that the initiation temperatures T_{in} match or are close to temperatures of the structural phase transformations T_K in the corresponding binary systems ($T_{in} = T_K$) [20–26, and the references therein]. Indeed, the initiation temperature T_{in} in Cu/Au bilayers coincides with the temperature $T_K = 240°C$ of the order–disorder phase transition in Cu–Au systems. The solid-state reactions in the Ni/Fe ($T_{in} = 350°C$) and Cu/Fe ($T_{in} = 850°C$) bilayers coincide with the temperatures of the eutectoid decompositions in Ni–Fe and Cu–Fe binary systems, respectively. The solid-state reactions in Cu/Ni ($T_{in} = 350°C$) and Ge/Mn ($T_{in} = 120°C$) thin films are associated with the existence of the spinodal decomposition in Cu–Ni and Ge–Mn systems, respectively. It is interesting to note that reactions also start at temperatures of diffusionless martensitic transformations. In fact, the low-temperature reactions in Ni/Al, Ti/Ni, Cd/Au, and Mn/Fe bilayers start at 180°C, $\sim 100°C$, 67°C, and 220°C, which are close to or coincide with the temperatures of the reverse martensitic transformations in Ni–Al, Ti–Ni, Cd–Au, and Mn–Fe binary systems, respectively. Moreover, the equality $T_{in} = T_K$ was also found for the eutectic reaction (420°C) in Al/Ge, the superionic transition (150°C) in Se/Cu bilayers, and other phase transformations [20–26].

All these facts prove that the same chemical interactions control both the chemical reactions and the corresponding solid-state structural transformations, with the consequence being the equality of the reaction initiation temperatures $T_{in}(A/B)$ in the A/B bilayers and the temperatures of the phase transformations T_k in the A–B binary systems. In summary, the equality $T_{in} = T_k$ indicates that solid-state thin-film reactions in A/B bilayers occur in A–B binary systems, with corresponding solid-state transformations. Generally speaking, there is a

one-to-one correspondence, $T_{in}^i = T_k^i$, between the initiation temperatures of compounds T_{in}^i in the phase sequence and the temperatures of phase transformations T_k^i in a given binary system. Therefore, the study of reactions with increasing annealing temperature in A/B bilayers made up of different layer ratios, which determine the composition of the alloys, is a study of the A–B phase diagram.

There have only been a few studies of phase formations at the solid-Fe/solid-Sn interface [27] in solid-Fe/liquid-Sn diffusion couples [28–30], Sn/Fe–Ni systems [31, 32] and Fe/Sn bilayers after ion irradiation [33]. In all cases, the $FeSn_2$ phase is formed at low temperatures, and this implies that $FeSn_2$ is the first phase formed at the Sn/Fe interface. However, there have been few investigations of the chemical reactions between the Fe and Sn layers and the sequential formation of the $Fe_{1-x}Sn_x$ phases at the Sn/Fe interface when the annealing temperature increases from room temperature to 800°C. In this work, we have described the solid-state reactions between polycrystalline Sn and epitaxial Fe(001) films and identified the phase sequences in 7Sn/93Fe(001) and 25Sn/75Fe(001) bilayers. Using X-ray diffraction, magnetic torque curve studies and scanning electron microscopy, we found that for both samples the non-magnetic first phase, $FeSn_2$, and the second phase, $FeSn$, were formed at $\sim 150°C$ and $\sim 300°C$, respectively at the Sn/Fe interface. Above 550°C, the ferromagnetic phases α-$Fe_{1-x}Sn_x$, Fe_5Sn_3 and Fe_3Sn_2 appeared in the reaction products, and there was no hard magnetic Fe_3Sn in the bulk samples.

Results

Structural evolution and magnetic transformations in the 9Sn/91Fe(001) bilayer during annealing at temperatures up to 800°C

Figure 1a shows a schematic diagram of the phase formation sequence that successively occurred in the 9Sn/91Fe(001) bilayers on a MgO(001) substrate during annealing at temperatures from room temperature to 800°C. Figure 1b shows the XRD profiles of the as-deposited 9Sn/91Fe(001) film and of the film after annealing at temperatures from room temperature to 800°C. The as-deposited samples show a strong Fe(002) peak, proving the epitaxial Fe(001) film growth on the MgO(001) substrate, and low diffraction peaks from the polycrystalline Sn, which are a signature of 9Sn/91Fe(001) bilayer formation and the lack of mixing and reaction between the Sn and Fe(001) layers. In all XRD patterns, there was a peak with an interplanar distance of 0.151 nm, which belongs to the (220) reflection of the solid $Mg_{1-x}Fe_xO_4$ solution. This clearly indicates that the $Mg_{1-x}Fe_xO_4$ interlayer is required for epitaxial growth of Fe(001) on the MgO(001). After annealing at temperatures above 150°C, the Sn peaks decreased significantly and reflections from the $FeSn_2$ occurred. This implies that $FeSn_2$ was the first phase formed

above the initial temperature $T_{in} \sim 150°C$ at the Sn/Fe interface, and only the Fe(002) and FeSn$_2$ peaks were present in the diffraction patterns at temperatures up to 300°C. After annealing at 300°C the peaks of the FeSn phase occurred, in addition to the FeSn$_2$, following the solid-state reaction FeSn$_2$ + Fe → (∼ 300°C) 2FeSn. Above 300°C and up to 550°C, there were FeSn and Fe(001) reflections in the diffraction patterns. After annealing at 550°C, the Fe (002) peak disappeared completely and a new epitaxial peak (002) of the α-Fe$_{1-x}$Sn$_x$ solid solution was formed, which remained up to 800°C. The interplanar spacing of the peak (002) increased with an increase in the annealing

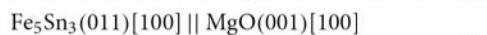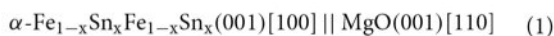temperature, which means an increase in the concentration of x of Sn in the α-Fe$_{1-x}$Sn$_x$ solid solution. According to Vegard's law [3]:

$$\alpha = (1 + 0.258(2) \times x) \times \alpha_{Fe}$$

where $\alpha_{Fe} = 0.2867$ nm, after annealing at 600°C, 700°C, 800°C, the Sn concentrations in the α-Fe$_{1-x}$Sn$_x$ solid solution were 3.9, 4.1, 4.5 at.% Sn, respectively. Above 600°C, the FeSn reflections disappear and new reflections with interplanar spacing 0.299 nm and 0.1495 nm begin to grow with increasing annealing temperature, implying epitaxial growth of the new phases. These reflections may belong to the hexagonal Fe$_5$Sn$_3$, the

Figure 1: (a) Schematic of the phase sequence 9Sn/91Fe(001) → (∼ 150°C) FeSn$_2$ → (∼ 300°C) FeSn → (∼ 550°C) α-Fe$_{1-x}$Sn$_x$ → (∼ 600°C) α-Fe$_{1-x}$Sn$_x$ + Fe$_5$Sn$_3$ + Fe$_3$Sn$_2$ → (∼ 700°C) α-Fe$_{1-x}$Sn$_x$ + Fe$_5$Sn$_3$ + α-Fe + β-Sn and (b) X-ray diffraction patterns in the epitaxial 9Rh/91Fe(001) bilayer during annealing at temperatures from room temperature up to 800°C.
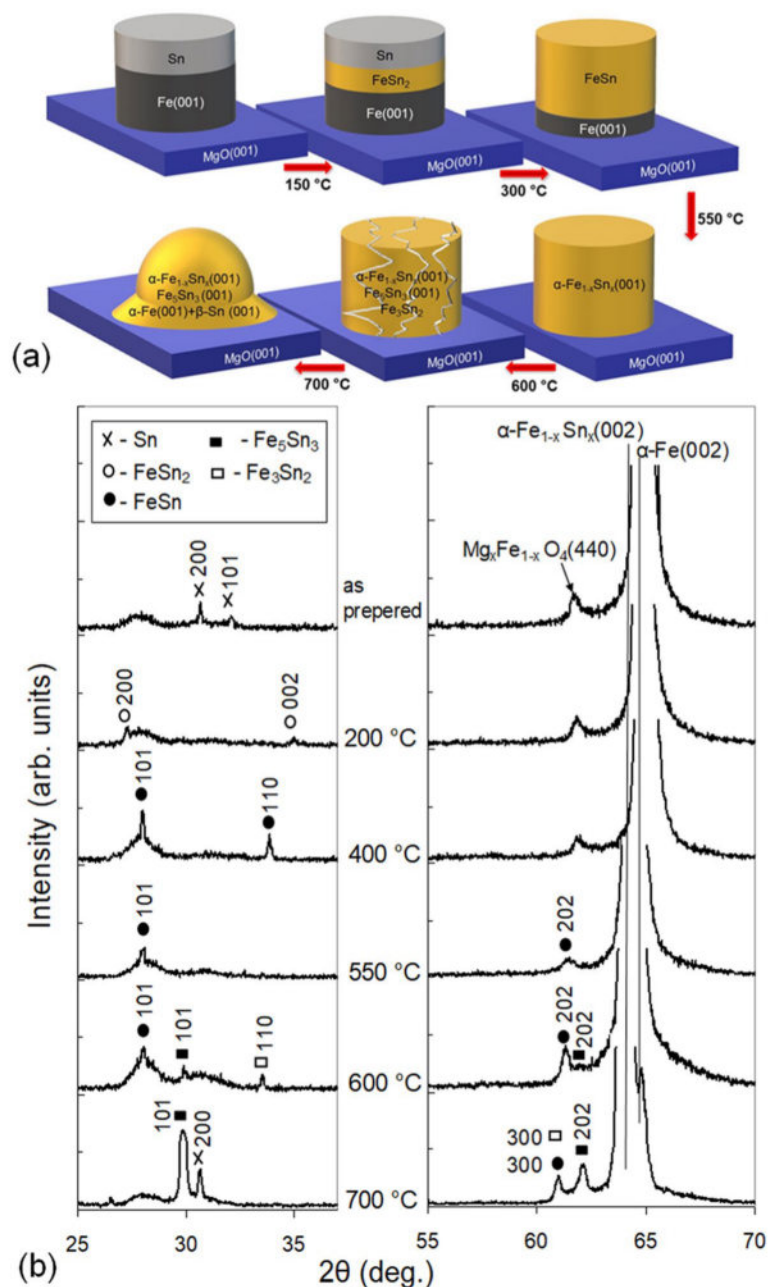
rhombohedral Fe_3Sn_2 or a new metastable $B2$-Fe_3Sn alloy [36]. However, the symmetric and asymmetric XRD scans showed the formation of the cubic α-$Fe_{1-x}Sn_x$ and hexagonal Fe_5Sn_3 phases. The XRD patterns contained only the $Fe_5Sn_3(011)$, $Fe_5Sn_3(022)$ and α-$Fe_{1-x}Sn_x$ (002) peaks, which indicates the parallel orientation of the $Fe_5Sn_3(011)$ and α-$Fe_{1-x}Sn_x$ (001) planes to the MgO(001) substrate. Asymmetric XRD scans for MgO, Fe_5Sn_3, and α-$Fe_{1-x}Sn_x$ were carried out using the (042), (030), and (032) reflections, respectively, and the orientation relationships (1) and (2) were identified. The schematic is presented in Fig. 2.

$$\alpha\text{-}Fe_{1-x}Sn_xFe_{1-x}Sn_x(001)[100] \parallel MgO(001)[110] \quad (1)$$

$$Fe_5Sn_3(011)[100] \parallel MgO(001)[100]$$
$$Fe_5Sn_3(011)[100] \parallel MgO(001)[010] \quad (2)$$

The formation of a mixture of α-$Fe_{1-x}Sn_x$ and Fe_5Sn_3 phases was also observed in bulk $Fe_{91}Sn_9$ samples after annealing at 750°C for 24 h [37]. In addition to α-$Fe_{1-x}Sn_x$ and Fe_5Sn_3, the $Fe_3Sn_2(110)$ phase epitaxially grew at temperatures between 600°C and 700°C, forming $Fe_3Sn_2(110)$ and $Fe_3Sn_2(220)$ reflections (Fig. 1b). Above 700°C, the peaks of Fe_3Sn_2 disappeared and, in addition to the peaks of α-$Fe_{1-x}Sn_x$ and Fe_5Sn_3, there was the formation of the peaks of (002)Sn and (002)α-Fe, which persisted up to 800°C. The presence of only the (002) β-Sn and (002) Fe reflections in the diffraction patterns indicates the epitaxial growth of β-Sn and α-Fe on the MgO(001) surface as a result of the partial decomposition of α-$Fe_{1-x}Sn_x$ or Fe_3Sn_2 into α-Fe + β-Sn above 700°C. To summarize, the chemical reaction between Fe and Sn began in the solid state at a low annealing temperature ($\sim$150°C), and with an increase in the annealing temperature up to 800°C the phase sequence (3) was formed.

$$9Sn/91Fe(001) \rightarrow (\sim 150\,°C)\, FeSn_2 \rightarrow (\sim 300\,°C)\, FeSn$$
$$\rightarrow (\sim 550\,°C)\alpha\text{-}Fe_{1-x}Sn_x \rightarrow (\sim 600\,°C)\alpha\text{-}Fe_{1-x}Sn_x$$
$$+ Fe_5Sn_3 + Fe_3Sn_2 \rightarrow (\sim 700\,°C)\alpha\text{-}Fe_{1-x}Sn_x + Fe_5Sn_3$$
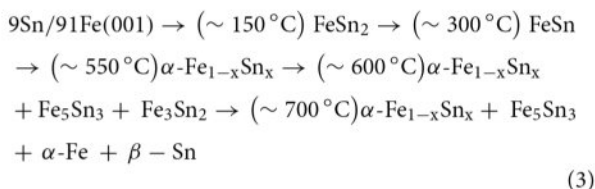$$+ \alpha\text{-}Fe + \beta - Sn$$
$$(3)$$

Figure 3a shows the dependence of the in-plane relative fourfold magnetic anisotropy constant $K_4(T_a)/K_4^0$ and of the relative magnetization $M_S(T_a)/M_S^0$ as a function of the annealing temperature T_a, where for the 9Sn/91Fe(001) samples $K_4^0 = 4.25\cdot10^5$ erg cm^3 and $M_S^0 = 1450$ emu/cm^3. The $K_4(T_a)/K_4^0$ and the $M_S(T_a)/M_S^0$ remained equal to one after annealing up to 150°C, confirming the absence of mixing and the formation of compounds at the Sn/Fe interface. Within experimental error, the relative anisotropy constant $K_4(T_a)/K_4^0$ and the relative magnetization $M_S(T_a)/M_S^0$ decreased identically as the annealing temperature increased for both the 150–300°C and 300–550°C temperature intervals. This is in good agreement with the XRD analysis, which showed the successive formation of the
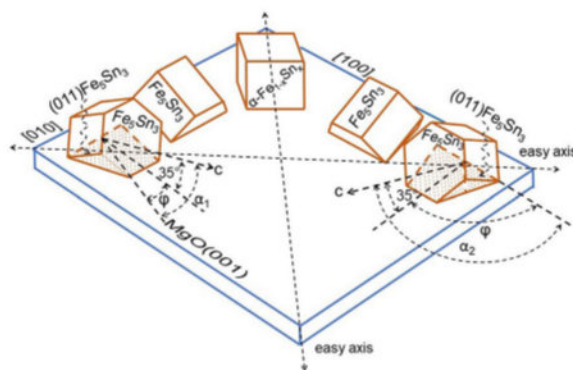
Figure 2: Schematic view of the four variants of the decagonal $Fe_5Sn_3(011)$ and cubic α-$Fe_{1-x}Sn_x$ (001) growing on the (001) surface of MgO, with their corresponding epitaxial relations (1) and (2). A set of four crystallite variants of the hexagonal $Fe_5Sn_3(011)$, like those of the cubic α-$Fe_{1-x}Sn_x$ (001), have in-plane fourfold anisotropy with an easy axis lying along the [110] and [110] directions of MgO (001).

non-ferromagnetic $FeSn_2$ and $FeSn$ phases in these temperature ranges. However, after annealing at temperatures above 550°C, the magnetization M_S decreased and the anisotropy constant K_4 sharply increased, with the final reaction products (α-Fe_{1-x} Sn_x + Fe_5Sn_3 + α-Fe + β-Sn), occurring in the temperature range 700–800°C, taking values of $M_S \sim 810$ emu/cm^3 ($M_S/M_S^0 \sim 0.55$) and $K_4 = 6\times10^5$ erg/cm^3 ($K_4(T_a)/K_4^0 \sim 1.4$) (Fig. 3a). According to the X-ray diffraction patterns (Fig. 1b), the formation of ferromagnetic phases began at 550°C with the synthesis of the phase α-$Fe_{0.96}Sn_{0.04}$, which at 600°C had a magnetization $M_S = 1130$ emu/cm^3 ($M_S/M_S^0 = 0.75$) and first magnetocrystallographic anisotropy constant K_1 ($Fe_{0.96}Sn_{0.04}$) = $K_4 = 5.6\times10^5$ erg/cm^3 ($K_4(T_a)/K_4^0 \sim 1.2$) (Fig. 3a). At a temperature of 650°C, the Fe_5Sn_3 and $Fe_{0.96}Sn_{0.04}$ phases coexisted, and they had a total magnetization of 930 emu/cm^3 ($M_S/M_S^0 = 0.64$) and fourfold constant $K_4(Fe_5Sn_{3\,+}\,Fe_{0.96}Sn_{0.04}) = 6\times10^5$ erg/cm^3 ($K_4(T_a)/K_4^0 \sim 1.4$). Taking the magnetization of Fe_5Sn_3 to be equal to 750 emu/cm^3 [1], it was easy to obtain a rough estimate of the fractions for Fe_5Sn_3 and $Fe_{0.96}Sn_{0.04}$ crystallites, which were $\sim$0.5. This made it possible to determine the contribution $K_4(Fe_5Sn_3) = 6.4\times10^5$ erg/cm^3 of the four variants of Fe_5Sn_3 (011) nanocrystals to the fourfold anisotropy constant $K_4(Fe_5Sn_3 + Fe_{0.96}Sn_{0.04})$. Figure 3b shows the in-plane hysteresis loop after annealing at 800°C, where the magnetic field was applied along the easy axis, which coincided with either the [110] or [110] direction of the MgO(001) substrate. The hysteresis loops had low coercivity $\sim$40 Oe, which means that the final reaction product ($Fe_5Sn_3 + Fe_{0.96}Sn_{0.04} + \alpha$-Fe) and hence each of the phases Fe_5Sn_3, $Fe_{0.96}Sn_{0.04}$ and α-Fe were ordinary soft magnetic materials.

We next discuss how the magnetic anisotropy behavior of the four variants of the $Fe_5Sn_3(011)$ nanocrystals relates to the

microstructure revealed by the orientation relationships (2). The magnetocrystalline anisotropy energy density for a hexagonal crystal E_K, excluding the basal plane anisotropy, is $E_K = E_0 + K_1 \sin^2\alpha + K_2 \sin^4\alpha$, where K_1 and K_2 are the first- and second-order anisotropy constants, respectively, and α is the angle between the magnetization M_S and the c-axis. For exchange-coupled Fe_5Sn_3 nanocrystallites with the c-axis projection coinciding with the [100] and [010] directions of the substrate MgO(001) and with equal-volume fractions $f_1 = f_2 = 0.5$, the anisotropy energy E_K in the spherical polar coordinates θ and φ (Fig. 2) is given by:

$$E_K = (K_1 \sin^2\alpha_1 + K_2 \sin^4\alpha_1) \cdot f_1$$
$$+ (K_1 \sin^2\alpha_2 + K_2 \sin^4\alpha_2) \cdot f_2$$
$$= E_0(\theta) - 1/4 K_2 \cos^4\theta \cdot \sin^2 2\varphi \quad (4)$$

For the hexagonal lattice Fe_5Sn_3, the angle $\theta \approx 35°$ is the angle of inclination of the c-axis to the (001) MgO plane. The in-plane anisotropy energy density $E_K^{\parallel}$, determined by $\theta \approx 35°$

(a)

(b)

Figure 3: (a) Relevant evolution of the magnetization M_S/M_S^0 and anisotropy constants $K_4(T_a)/K_4^0$ as a function of the annealing temperature, showing the low-temperature formation of the polycrystalline non-magnetic FeSn (~ 150°C) and $FeSn_2$ (~ 300°C) and their transformation into the epitaxial α-$Fe_{1-x}Sn_x$ (001), Fe_5Sn_3(011), Fe(001), and α-Fe(001) above 550°C. (b) In-plane hysteresis loops of 9Sn/91Fe(001) bilayer films annealed at 800°C, showing that α-$Fe_{1-x}Sn_x$, Fe_5Sn_3, and α-Fe are soft magnetic phases.

(Fig. 2) in expression (1) and therefore K_2, is easy to find using an in-plane torque curve $L^{\parallel}(\varphi)$ (4).

$$L_{\parallel}(\varphi) = \partial E_K/\partial\varphi = -1/2 K_2 \cos^4 35° \sin 4\varphi = -0.225 K_2 \sin 4\varphi \quad (5)$$

In expression (5), the in-plane anisotropy energy has a "minus" sign, indicating that for $K_2 > 0$ the easy axes of the in-plane anisotropy should coincide with the [110] and [110] directions of MgO(001) (Fig. 2). It follows from this that the four variants of the hexagonal lattice Fe_5Sn_3 (011) (Fig. 2) had a fourfold anisotropy constant $K_4(Fe_5Sn_3) = -0.225 K_2(Fe_5Sn_3) = 6.4 \times 10^5$ erg/cm³. Hence, it follows that the second constant of the magnetic anisotropy K_2 (Fe_5Sn_3) was equal to 2.8×10^6 erg/cm³. The perpendicular anisotropy constant $K_\perp = 2\pi Ms^2 \pm \Delta K_\perp$ is comprised of the shape anisotropy and the $\Delta K_\perp$ contribution, which is a function of the first magnetocrystalline constant $K_1(Fe_5Sn_3)$. In particular, the calculation showed that $\Delta K_\perp = K_1(Fe_5Sn_3)$ for exchange-bound hexagonal Fe_5Sn_3(110) nanocrystals with the c-axis lying along the [100] and [010] directions in the (001) plane of the MgO substrate. In contrast, for the four variants of the Fe_5Sn_3(011) nanocrystals, it was difficult to obtain an analytical expression of $\Delta K_\perp$ as a function of the constant $K_1(Fe_5Sn_3)$. This is because above 600°C the films contained a mixture of Fe_5Sn_3 and $Fe_{1-x}Sn_x$ phases, the c-axes of Fe_5Sn_3(011) crystallites did not lie in the film plane, and the films did not remain continuous, breaking up into magnetic isolated islands (Fig. 6) by solid-state dewetting. However, these films had in-plane anisotropy, and rough estimates showed that $\Delta K_\perp > 0$, which suggests that the easy axis is the c-axis ($K_1(Fe_5Sn_3) > 0$) and did not lie in the basal plane ($K_1(Fe_5Sn_3) < 0$). Our data do not agree with the results of [1, 8], in which $K_1(Fe_5Sn_3) < 0$ and the values of the constant $K_2(Fe_5Sn_3)$ were close to zero [8].

Thus, magnetic measurements of the 9Sn/91Fe (001)/MgO (001) thin films showed the formation of a mixture of ferromagnetic epitaxial Fe_5Sn_3(011) and α-$Fe_{96}Sn_4$(001) phases in the temperature range of 600–700°C, which had a common magnetization of 930 emu/cm³ and fourfold constant $K_4 = 6 \times 10^5$ erg/cm³, with the easy axes coinciding with the [110] and [110] directions of the MgO (001) substrate.

Structural and magnetic transformations in the 25Sn/75Fe(001) bilayer during annealing at temperatures up to 800°C

Figure 4a shows a schematic diagram of the phase formation sequence that successively occurred in the 25Sn/75Fe(001) bilayers on a MgO(001) substrate during annealing at temperatures from room temperature to 800°C. Like the 7Sn/93Fe (001) bilayers, the X-ray diffraction patterns of the 25Sn/75Fe (001) bilayers showed that $FeSn_2$ started at 150°C, which reacted with the residual Fe (001) layer above 300°C to form
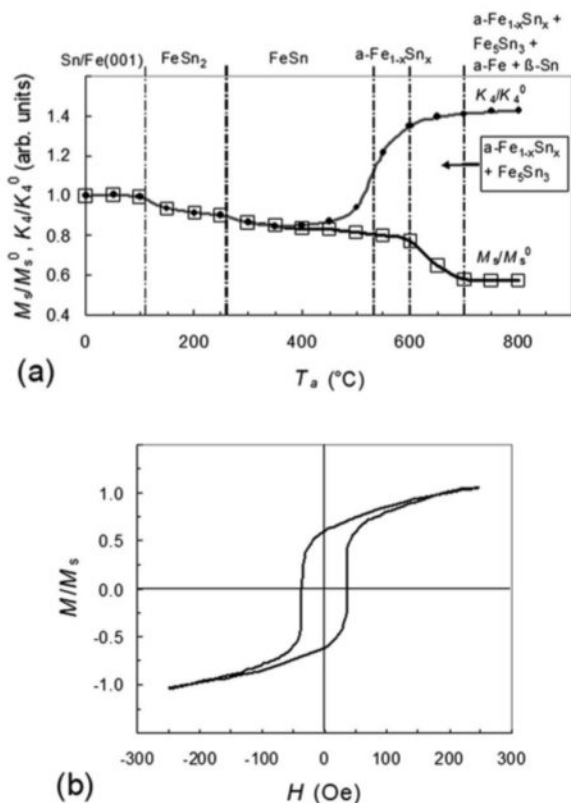
the FeSn phase (Fig. 4b). After annealing at 550°C, only FeSn and α-Fe were present in the reaction products. After annealing at 550°C, the (002)Fe peak was replaced by the epitaxial (002) peak of the α-Fe$_{1-x}$Sn$_x$ solid solution, which completely disappeared at 600°C. Above 600°C low reflections of Fe$_5$Sn$_3$ and Fe$_3$Sn$_2$ appeared in addition to the FeSn peaks, slightly increasing up to 800°C. Weak reflections of β-Sn appeared after annealing at 700°C, and thus the reaction products after annealing at 800°C contained a mixture of phases, FeSn + Fe$_3$Sn$_2$ + Fe$_5$Sn$_3$ + β-Sn. It is important to emphasize that there were no reflections of the Fe$_3$Sn phase, which was expected in the 9Sn/91Fe (001) and 25Sn/75Fe (001) bilayers.

Overall, the phase sequence (6) formed after annealing the 25Sn/75Fe(001) bilayers at temperatures up to 800°C was:

$$25Sn/75Fe(001) \rightarrow (\sim 150\,°C)\,FeSn_2 \rightarrow (\sim 300\,°C)$$
$$FeSn \rightarrow (\sim 550\,°C)\,FeSn + \alpha\text{-}Fe_{1-x}Sn_x \rightarrow (\sim 600\,°C)$$
$$FeSn + Fe_3Sn_2 + Fe_5Sn_3 \rightarrow (700°C)FeSn + Fe_3Sn_2$$
$$+ Fe_5Sn_3 + \beta - Sn$$

$$(6)$$

Figure 5a shows the dependence of the in-plane relative magnetic anisotropy constant $K_4(T_a)/K_4^0$ and of the relative magnetization $M_S(T_a)/M_S^0$ as a function of the annealing temperature T_a, where for the 25Sn/75Fe(001) samples,

Figure 4: (a) Schematic of the phase transformations in the 25Rh/75Fe(001) bilayer showing the polycrystalline FeSn$_2$ and FeSn and the epitaxial α-Fe$_{1-x}$Sn$_x$(001) phase formation at 150°C, 300°C, and 550°C, respectively. (b) Temperature-dependent X-ray diffraction patterns in the epitaxial 25Rh/75Fe(001) bilayer during annealing at temperatures from room temperature up to 800°C.

$K_4^0 = 2.8 \cdot 10^5$ erg/cm^3 and $M_S^0 = 960$ emu/cm^3. These dependences are in good agreement with the results of the XRD analysis. The values of $K_4(T_a)/K_4^0$ and $M_S(T_a)/M_S^0$ remained equal to one after annealing at temperatures up to 150°C, confirming the absence of mixing and the formation of compounds at the Sn/Fe interface. Within experimental error, the relative anisotropy constant $K_4(T_a)/K_4^0$ and the relative magnetization $M_S(T_a)/M_S^0$ decreased identically as the annealing temperature increased for both the 150–300°C and 300–600°C temperature intervals. This was in good agreement with the successive formation of the non-ferromagnetic FeSn$_2$ and FeSn phases in these temperature ranges. However, after annealing at temperatures above 600°C, the magnetization M_S slightly increased, reaching ~125 emu/cm^3 ($M_S/M_{S0} \sim 0.13$) at 800°C, with a corresponding anisotropy constant of $K_4 = 0$ (Fig. 5a). Figure 5b shows the hysteresis loops had low coercivity ~20 Oe, which means that the final reaction products (FeSn + Fe$_3$Sn$_2$ + Fe$_5$Sn$_3$ + β-Sn) were soft magnetic materials. The X-ray diffraction patterns, low values of the magnetization and the absence of anisotropy indicate the formation of small amounts of the polycrystalline ferromagnetic Fe$_5$Sn$_3$, Fe$_3$Sn$_2$ and Sn phases in the final reaction products, in addition to the basic FeSn.

Dewetting of 9Sn/91Fe(001) and 25Sn/75Fe(001) thin films

The 9Sn/91Fe(001) and 25Sn/75Fe(001) thin films on the MgO(001) substrate remained continuous until annealing at 550°C (Fig. 6a, Fig. 7a). Nevertheless, above 550°C, the film structure became unstable and, by solid-state dewetting [38–40], was rearranged into interconnected structures (Fig. 6b, Fig. 7b), finally breaking up into isolated islands at 800°C (Fig. 6c, Fig. 7c). Scanning electron microscopy showed that the sample morphology depended on the composition: after annealing the dewetting 9Sn/91Fe(001) bilayer at 800°C, the islands became semi-spherical (Fig. 6d); at the same annealing temperature, they became close to spherical for the 25Sn/75Fe(001) bilayer (Fig. 7d). It is important to note that in the 9Sn/91Fe(001) films, the atomic transport during solid-state dewetting and formation of micron-sized islands from the 300 nm films did not lead to structural disorder but preserved the orientation of the epitaxial α-Fe$_{1-x}$Sn$_x$ (001), Fe$_5$Sn$_3$(011) and Fe(001) phases. This implies that the atomic transport by dewetting was not due to a random diffusion process, but was rather associated with chemical interactions that occurred during solid-phase transformation. Dewetting started in the 9Sn/91Fe(001) and 25Sn/75Fe(001) bilayers at temperatures above 550°C and finished at 800°C. In the temperature range 550–800°C, the phase sequences (1) and (2) showed consistent formation of the α-Fe$_{1-x}$Sn$_x$, Fe$_5$Sn$_3$, Fe$_3$Sn$_2$,

α-Fe, and β-Sn phases. This strongly suggests that the same chemical mechanisms controlled both the synthesis of these phases and the solid-state dewetting process. This hypothesis is consistent with the effects of alloying on solid-state dewetting of Au/Ni bilayers [41]. A rough estimation of the radius r of the film surface required to form one island, as shown in Fig. 6c and Fig. 7c, gave r ~ 2μ. This suggests that the atoms migrated in typical annealing time t = 4 × 10^3 s over a distance of at least 2×10^{-4} cm, which corresponded to the effective diffusion coefficient $D^{eff} = r^2/t \sim 10^{-11}$ cm^2/s. The actual value of D^{eff} could be several orders of magnitude higher and closer to the value of the diffusion coefficient at the melting threshold, which was ~ 10^{-8} cm^2/s. In addition, the EDS spectra showed a change in the composition of the initial 9Sn/91Fe films to Sn$_{17}$Fe$_{83}$ and 25Sn/75Fe films to Sn$_{50}$Fe$_{50}$ with increasing temperatures up to 800°C. This might be due to partial Fe sublimation. Recently, S. Kunwar et al. reported that Ag atom sublimation played a significant role in the solid-state dewetting process of Ag/Au/Pt trilayers [42]. It is important to note that after annealing at 800°C, the 9Sn/91Fe (001) and 25Sn/75Fe (001) bilayers showed typical in-plane hysteresis loops (Fig. 3b, Fig. 5b) whose shapes were close to the shape
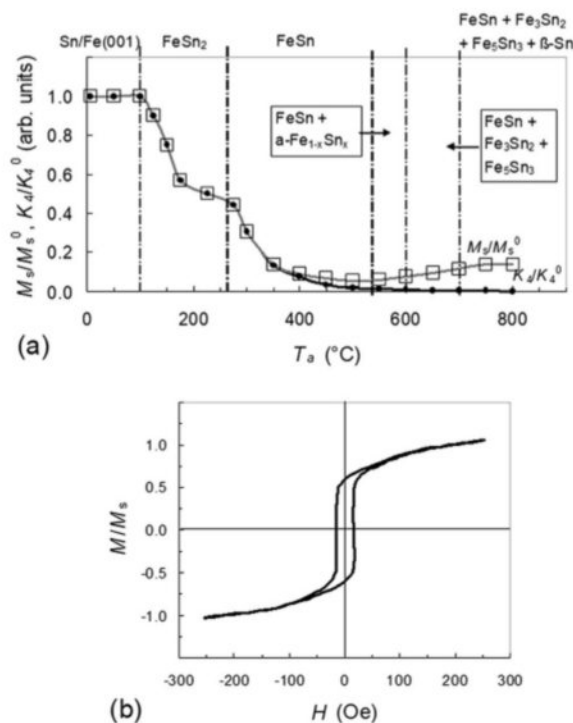

Figure 5: (a) Relevant evolution of the magnetization M_S/M_S^0 and anisotropy constants $K_4(T_a)/K_4^0$ confirming the sequential formation 25Sn/75Fe(001) → (~ 150°C) FeSn$_2$ → (~ 300°C) FeSn → (~ 550°C) FeSn + α-Fe$_{1-x}$Sn$_x$ → (~ 600°C) FeSn + Fe$_3$Sn$_2$ + Fe$_5$Sn$_3$ → (700°C) FeSn + Fe$_3$Sn$_2$ + Fe$_5$Sn$_3$ + β-Sn. (b) In-plane hysteresis loops of 25Rh/75Fe(001) bilayer films annealed at 800°C, confirming that Fe$_3$Sn$_2$ and Fe$_5$Sn$_3$ are soft magnetic phases.
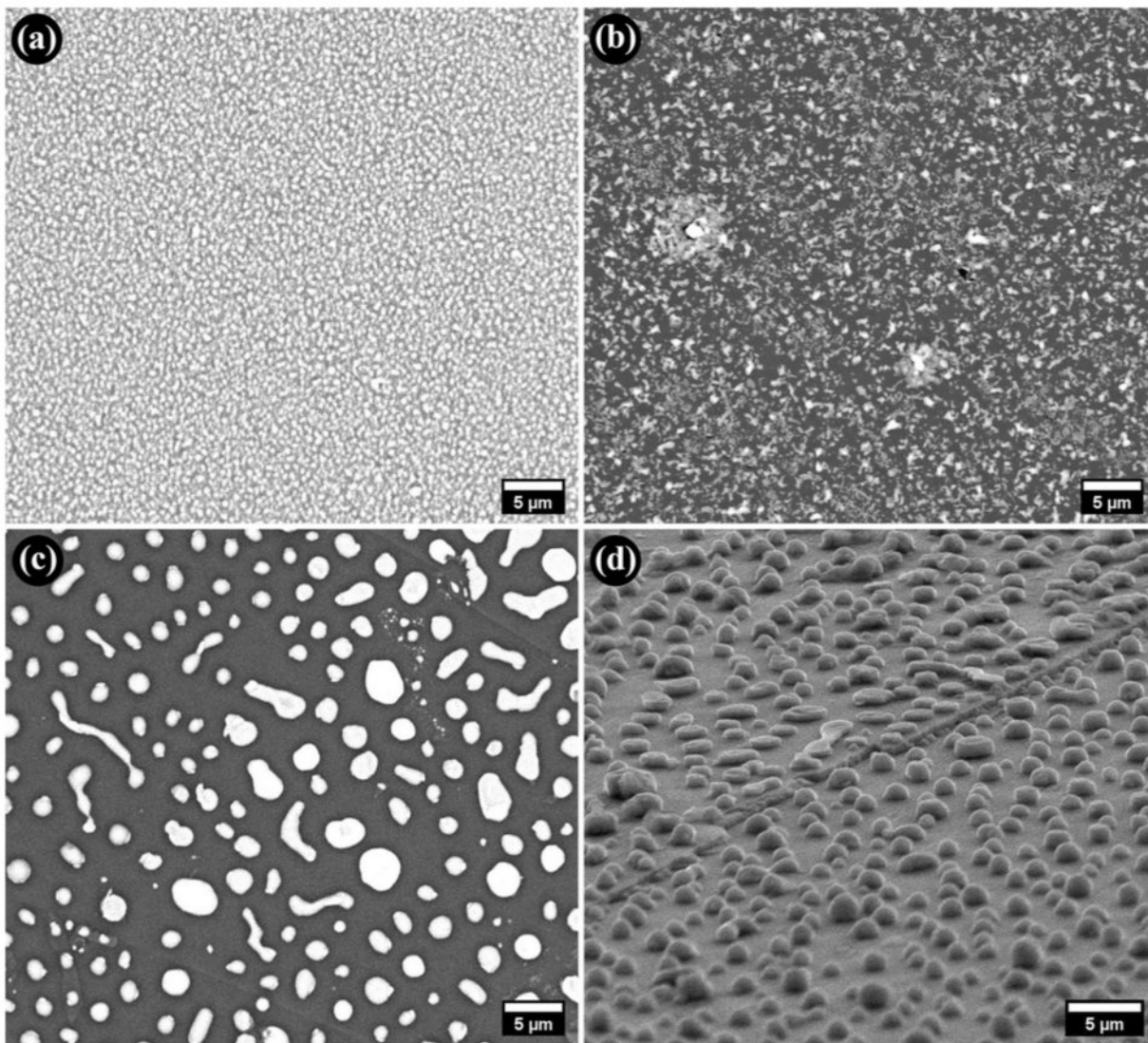
Figure 6: SEM images showing the morphological evolution: (a) as-deposited compact 7Sn/93Fe(001) bilayer film completely covering the substrate MgO(001), (b) during solid-state dewetting after annealing at 600°C into interconnected structures, (c) isolated islands at 800°C, (d) the final reaction products after annealing at 800°C are micrometer-sized semi-spherical epitaxial (α-Fe$_{1-x}$Sn$_x$ (001) + Fe$_5$Sn$_3$(011) + α-Fe(001) + β-Sn(001)) islands possessing common magnetization 940 emu/cm^3 and fourfold constant $K_4 = 6 \times 10^5$ erg/cm^3.

of the hysteresis loop ensemble of single-domain particles described by the Stoner–Wohlfarth theory. This result confirms that the final reaction products of both samples contained separate non-interacting islands.

Based on the data presented, the following hypothetical model of the dewetting process of the samples was proposed. There were chemical interactions in 9Sn/91Fe (001) and 25Sn/75Fe (001) samples at temperatures above 550°C that increased the atomic mobility, converting the film from a solid to a quasi-liquid state and controlling not only the phase transformations but also the overall dewetting process. In particular, these interactions broke the bonds between the film and the substrate, collected the film material by coherent

atomic transfer without disturbing the epitaxy into islands, and created the partial Fe sublimation.

Finally, the X-ray diffractions, torque measurements and SEM images showed that the dewetted 9Sn/91Fe(001) bilayers were epitaxial Fe$_5$Sn$_3$ (011) + α-Fe$_{1-x}$Sn$_x$ (001) + Fe(001) + Sn(001) semi-spherical island films of saturation magnetization ~ 930 emu/cm^3 and fourfold magnetic anisotropy $K_4 = 6 \times 10^5$ erg/cm^3. In contrast to the 9Sn/91Fe (001) bilayers, the dewetted 25Sn/75Fe (001) bilayers were spherical island films of low magnetization ~ 125 emu/cm^3 and contained the main FeSn and a mixture of polycrystalline Fe$_3$Sn$_2$ + Fe$_5$Sn$_3$ + β-Sn phases. Both samples had
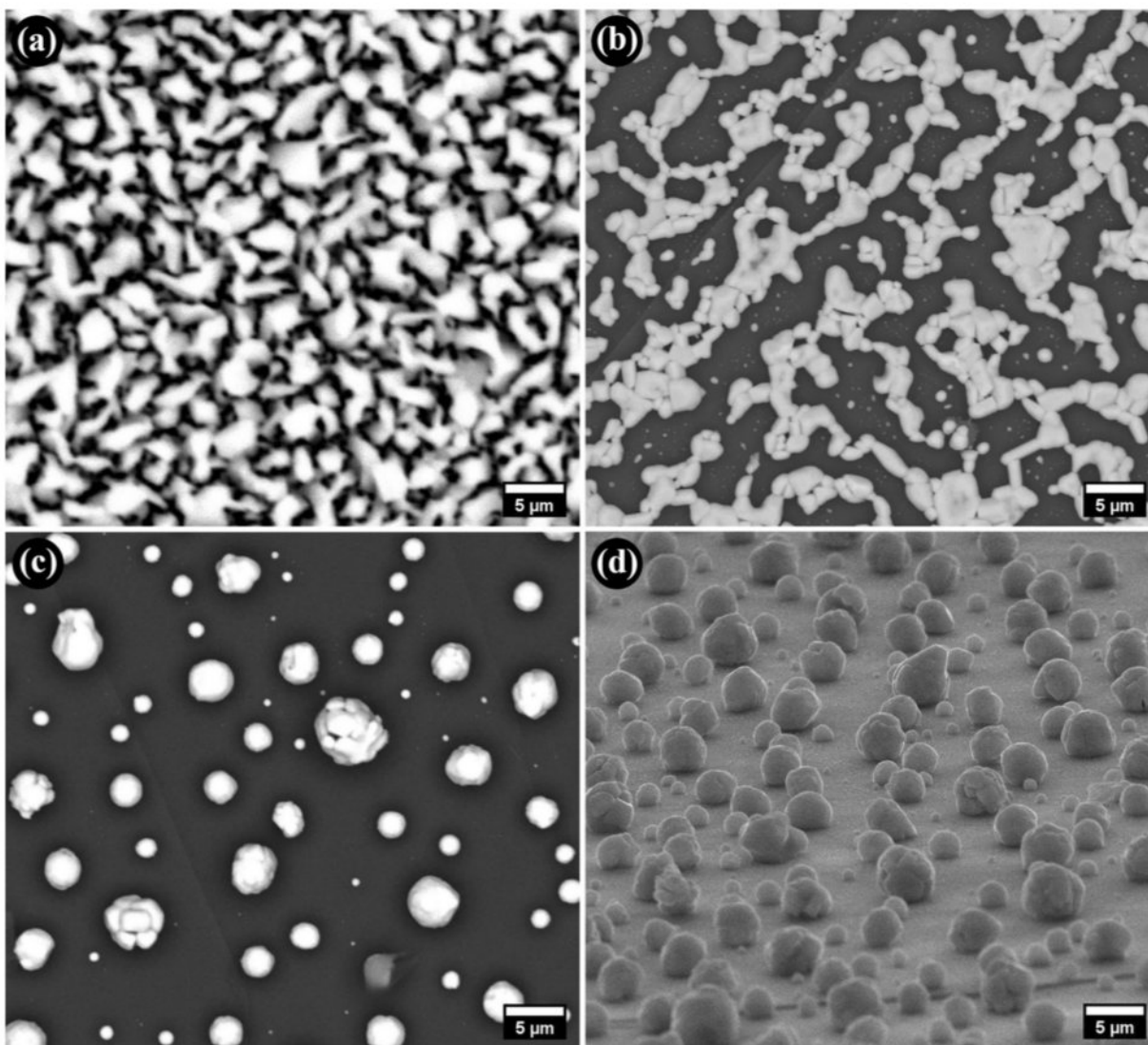
Figure 7: SEM images showing the morphological evolution: (a) as-deposited 25Sn/75Fe(001) bilayer film, (b) solid-state dewetting after annealing at 600°C, (c) 800°C, (d) the final reaction products after annealing at 800°C are micrometer-sized spherical polycrystalliine (FeSn + Fe$_3$Sn$_2$ + Fe$_5$Sn$_3$ + β-Sn) isolated magnetically soft islands, having a low value of magnetization ~ 125 emu/cm^3.

high electrical resistivity ~ 10^5 Ω·m and optical transmittance ~ 70–80% in the visible spectrum.

Discussion

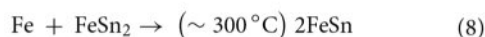### Phase sequences in Sn/Fe(001) bilayers and the phase diagram of Fe–Sn

At present the equilibrium phase diagram of binary metallic systems is built by cooling the melt to room temperature (top-down approach). As a result of extremely low diffusion coefficients, the low-temperature part of many phase diagrams is often either unknown or poorly established. In contrast, the phase sequence in thin-film solid-state reactions is obtained by heating bilayers from room temperature to high temperatures (bottom-up approach). Therefore, the interfacial reaction technique can be a powerful tool for research and clarification, especially for the low-temperature part of the phase diagrams. As shown above, the phase sequences (1) and (2) had initiation temperatures $T_{in}^1 = $ ~ 150°C, $T_{in}^2 = $ ~ 300°C, $T_{in}^3 = $ ~ 550°C, $T_{in}^4 = $ ~ 600°C, $T_{in}^7 = $ ~ 700°C. Following the equality $T_{in}^i = T_K^i$, the temperatures T_{in}^i are associated with the structural transformation temperatures T_K^i that should be indicated in the phase equilibrium

diagram of Fe–Sn. However, the T_{in}^{i} temperatures have not been precisely established, and some of them may coincide with the established temperatures of phase transformations in the Fe–Sn system. For the phase equilibrium diagram of Fe–Sn, the structural and magnetic properties of phases obtained by top-down approaches are constantly being refined [8, 9]. Recently, reactive crucible melting has been used to search for new phases in the Fe–Sn system [9]. This method consists of the fact that the original pure elements are annealed for a long time at high temperatures to carry out a reactive diffusion process and are then subsequently furnace-cooled at 5 K/min to room temperature or quenched to stabilize the high-temperature phases. Unexpectedly, it turned out that in the samples of $Fe_{70}Sn_{30}$, the Fe_5Sn_3 phase was absent in the diffusion zone of the reactive crucible, although it existed in the conventionally prepared homogenous samples (still of $Fe_{70}Sn_{30}$) above 800°C [9]. In contrast to this, we observed Fe_5Sn_3 formation at temperatures above 600°C, but did not detect the Fe_3Sn phase by magnetic and X-ray studies even after annealing at above 800°C, which was expected for these compositions. Therefore, further studies of solid-phase reactions in Sn/Fe films that are based on the composition and precise determination of the initiation temperatures are required for deep understanding of the phase formation in the high-temperature part of the Sn–Fe system.

Prediction of the phase transition at 150 °C and 300 °C

Below we will only discuss the possibility of phase transformations at the initiation temperatures $T_{in}^{1} \sim 150°C$, of the synthesis of the $FeSn_2$ phase, and $T_{in}^{2} \sim 300°C$, of the synthesis of the FeSn phase, which correspond to reactions (7) and (8) and are absent in the Fe–Sn phase diagram.

$$Fe \: + \: 2Sn \: \rightarrow \: (\sim 150 \,°C) \: FeSn_2 \qquad (7)$$

$$Fe \: + \: FeSn_2 \: \rightarrow \: (\sim 300 \,°C) \: 2FeSn \qquad (8)$$

The equality $T_{in}^{1} = T_{K}^{1}$ assumed the following scenario for $FeSn_2$ synthesis and phase transformation at $\sim 150°C$. When the temperature rose above $T_{in}^{1} \sim 150°C$, strong chemical interactions occurred between the reacting atoms at the Sn/Fe interface, leading to the breaking of chemical bonds in one of the layers (Sn or Fe), the transfer of one type of atom, which was the dominant diffusing species to the other layer (Fe or Sn), and the synthesis of $FeSn_2$, following reaction (7). From the equality $T_{in}^{1} = T_{K}^{1}$, it follows that $T_{in}^{1} \sim 150°C$ was also the temperature of the phase transformation, which was associated with the structural features of the $FeSn_2$ phase. With a decrease in temperature below $T_{in}^{1} \sim 150°C$, following the reverse reaction (7), the $FeSn_2$ phase tended to nano-separate into the original Fe and

Sn components. However, the formed chemical bonds did not allow for the destruction of the $FeSn_2$ lattice, and therefore the chemical interactions tended to form Fe and Sn nanoclusters within the $FeSn_2$ lattice. This could lead to a change of the order parameter, as in the order–disorder phase transformation, or to a slight distortion of the lattice, as in the martensitic transformation. Moreover, we have presented a possible scenario where chemical interactions can induce phase separation by spinodal nanodecomposition of $FeSn_2$ to Fe-rich $FeSn_2$ and Sn-rich $FeSn_2$ nanoclusters. The equality $T_{in}^{2} = T_{K}^{2}$ predicts a phase transformation at $T_{in}^{2} \sim 300°C$, which was associated with the structural features of the FeSn formation. Such a transformation could be the order–disorder phase transition in FeSn or the eutectoid transformation where the FeSn was synthesized by a reverse eutectoid reaction (8).

Although the phase transformations at $\sim 150°C$ and $\sim 300°C$ have been predicted, the structural origin of the phase transformations remains unknown. Despite the great scientific and practical importance, the proof and investigations of the spinodal decomposition and other phase transformations at low temperatures is known to be a complex experimental problem [43].

Conclusions

We have reported on phase sequences formed by solid-state synthesis in 9Sn/91Fe (001) and 25Sn/75Fe (001) bilayers upon annealing at temperatures up to 800°C. Above 600°C, both sequences were found to contain magnetic $\alpha\text{-}Fe_{1-x}Sn_x$ and Fe_5Sn_3 phases, but did not contain the hard magnetic Fe_3Sn phase, which was expected for these samples. Above 550°C, the process of dewetting began in both samples, and at 800°C the 9Sn/91Fe (001) bilayers formed islands containing the epitaxial $\alpha\text{-}Fe_{1-x}Sn_x(001) + Fe_5Sn_3(011) + \alpha\text{-}Fe(001) + \beta\text{-}Sn(001)$ phases, whereas the islands of 25Sn/75Fe (001) bilayers contained the basic polycrystalline FeSn and additional $Fe_3Sn_2 + Fe_5Sn_3 + \beta\text{-}Sn$ phases. The constant of magnetic anisotropy K_1 and the saturation magnetization of the $\alpha\text{-}Fe_{0.96}Sn_{0.04}$ alloys were determined and the constants K_1 and K_2 of the Fe_5Sn_3 phase were estimated. Phase sequences in 9Sn/91Fe(001) and 25Sn/75Fe(001) bilayers began with the formation of the $FeSn_2$ and FeSn phases at temperatures of $\sim 150°C$ and $\sim 300°C$, respectively. The analysis of many thin-film solid-state reactions suggested the existence of solid-state transformations at temperatures of $\sim 150°C$ and $\sim 300°C$ in the Sn–Fe system, which are absent in the phase equilibrium diagram. Finally, our approach was versatile and can be used for research and refinement of the phase equilibrium diagram (especially of the low-temperature part), not only of the Fe–Sn system, but of any binary system.

Experimental procedures

In the first step, the Fe(001) layers were epitaxially grown on a MgO(001) substrate at a pressure of 10^{-6} Torr and a temperature of 250°C, leading to the formation of the orientation relationship Fe(001)[100] || MgO(001)[110]. The Fe(001)/MgO(001) films had a saturation magnetization of ~ 1710 emu/cm³ and the first magnetocrystalline anisotropy constant was $K_1^{Fe} = 5.1 \cdot 10^5$ erg/cm³ for the bulk samples. In the second step, the top Sn layer was deposited at room temperature to prevent a reaction between Sn and Fe during the deposition. In the experiments, 2 samples, 7Sn/93Fe(001)/MgO(001) and 25Sn/75Fe(001)/MgO(001), with stoichiometries of Sn_7Fe_{93} and $Sn_{25}Fe_{75}$, respectively, determined by energy-dispersive X-ray spectroscopy (EDS) microanalysis and with total thickness up to 300 nm, were used. Initial samples were annealed for 1 h from 50°C to 800°C with a step size of 50°C. The magnetic in-plane fourfold anisotropy constants, K_4^0, and the saturation magnetizations, M_S^0, were determined for the total volume of the bilayers, which turned out to be $K_4^0 = 4.25 \cdot 10^5$ erg/cm³, $M_S^0 = 1450$ emu/cm³ for the 7Sn/93Fe(001) bilayers and $K_4^0 = 2.8 \cdot 10^5$ erg/cm³, $M_S^0 = 960$ emu/cm³ for the 25Sn/75Fe(001) bilayers. The formed phases were identified with a DRON-4-07 diffractometer (CuK_α radiation). The epitaxial film orientations were analyzed by means of asymmetrical XRD scans performed on a PANalytical X'Pert PRO diffractometer (Almelo, The Netherlands) with a PIXcel detector. The saturation magnetization, M_S, and the perpendicular anisotropy constant, $K_\perp = 2\pi M_s^2 \pm \Delta K_\perp$, were measured on a torque magnetometer with a sensitivity of $3.76 \cdot 10^{-9}$ Nm in the applied field range of 0–16 kOe using the method presented in [34]. The value of $\Delta K_\perp$ has been associated with the presence of in-plane strains and grain growth textures in thin films [34, 35]. If $\Delta K_\perp > 0$, then this indicates the existence of factors that, together with the shape anisotropy, place the easy axis in the film plane. In contrast, if $\Delta K_\perp < 0$, then these factors reduce the shape anisotropy, and when $K_\perp = 2\pi M_s^2 - \Delta K < 0$, the easy axis is aligned perpendicularly to the film plane. The fourfold anisotropy constant K_4 was determined from an in-plane torque curves $L_\parallel(\varphi)$ obtained in a magnetic field of 10 kOe. Scanning electron microscopy (SEM) and EDS analysis were performed to investigate the morphology and chemical composition of the deposited films. Top-view SEM images of the samples were obtained using a Hitachi TM4000Plus instrument (Tokyo, Japan) operated at an acceleration voltage of 20 kV and a high vacuum BSE (backscattered-electron) regime. Tilted-view SEM images of the samples were obtained using a UVD (ultra-variable-pressure) detector and a Hitachi SU3500 instrument (Tokyo, Japan) operated at an acceleration voltage of 5 kV and a low vacuum regime. No metal films were coated on the sample surface prior to taking the SEM measurement since all the samples were sufficiently electrically conductive.

Acknowledgments

Data availability

The data are available upon reasonable request from the corresponding author (VGM).

References

1. B.C. Sales, B. Saparov, M.A. McGuire, D.J. Singh, D.S. Parker, Ferromagnetism of Fe₃Sn and alloys. Sci. Rep. **4**, 7024 (2014)

2. C. Echevarria-Bonet, N. Iglesias, J.S. Garitaonandía, D. Salazar, G.C. Hadjipanayis, J.M. Barandiaran, Structural and magnetic properties of hexagonal Fe₃Sn prepared by non-equilibrium techniques. J. Alloys Compd. **769**, 843–847 (2018). https://doi.org/10.1016/j.jallcom.2018.07.257

3. H. Giefers, M. Nicol, High pressure X-ray diffraction study of all Fe–Sn intermetallic compounds and one Fe–Sn solid solution. J. Alloys Compd. **422**, 132–144 (2006). https://doi.org/10.1016/j.jallcom.2005.11.061

4. H. Li, B. Ding, J. Chen, Z. Li, Z. Hou, E. Liu, H. Zhang, X. Xi, G. Wu, W. Wang, Large topological Hall effect in a geometrically frustrated kagome magnet Fe₃Sn₂. Appl. Phys. Lett. **114**, 192408 (2019). https://doi.org/10.1063/1.5088173

5. Q. Wang, S. Sun, X. Zhang, F. Pang, H. Lei, Anomalous Hall effect in a ferromagnetic Fe₃Sn₂ single crystal with a geometrically frustrated Fe bilayer Kagome lattice. Phys. Rev. B **94**, 075135-1–075135-5 (2016). https://doi.org/10.1103/PhysRevB.94.075135

6. H. Li, B. Ding, J. Chen, Z. Li, E. Liu, X. Xi, G. Wu, Large anisotropic topological Hall effect in a hexagonal non-collinear magnet Fe₅Sn₃. Appl. Phys. Lett. **116**, 182405-1–182405-5. (2020). https://doi.org/10.1063/5.0005493

7. H. Li, B. Zhang, J. Liang, B. Ding, J. Chen, J. Shen, Z. Li, E. Liu, X. Xi, G. Wu, Y. Yao, H. Yang, W. Wang, Large anomalous Hall effect in a hexagonal ferromagnetic Fe5Sn3 single crystal. Phys. Rev. B **101**, 140409(R)-1-140409(R)-6 (2020). https://doi.org/10.1103/PhysRevB.101.140409.

8. B. Fayyazi, K.P. Skokov, T. Faske, I. Opahle, M. Duerrschnabel, T. Helbig, I. Soldatov, U. Rohrmann, L. Molina-Luna, K. Güth, H. Zhang, W. Donner, R. Schafer, O. Gutfleisch, Experimental and computational analysis of binary Fe-Sn ferromagnetic compounds. Acta Mater. **180**, 126–140 (2019). https://doi.org/10.1016/j.actamat.2019.08.054

9. B. Fayyazi, K.P. Skokov, T. Faske, D.Y. Karpenkov, W. Donner, O. Gutfleisch, Bulk combinatorial analysis for searching new rare-earth free permanent magnets: reactive crucible melting applied to the Fe-Sn binary system. Acta Mater. **141**, 434–443 (2017). https://doi.org/10.1016/j.actamat.2017.09.036

10. D. Goll, R. Loeffler, J. Herbst, C. Frey, S. Goeb, T. Grubesa, D. Hohs, A. Kopp, U. Pflanz, R. Stein, G. Schneider, Magnetic properties of hard magnetic (Fe, Cr)3S$_n$2 intermetallic compound. Phys. Stat. Sol. (RRL) **9**, 603–606 (2015). https://doi.org/10.1002/pssr.201510243

11. Y. Wan, J. Liu, C. Liu, S. Ji, Y. Zhou, Facile synthesis of FeSn$_2$ alloy nanoparticles as anode materials for lithium-ion batteries. Energy Environ. Focus **2**, 63–67 (2013). https://doi.org/10.1166/eef.2013.1027

12. J. Leibowitz, E. Allcorn, A. Manthiram, FeSn$_2$-TiC nanocomposite alloy anodes for lithium ion batteries. J. Power Sources **295**, 125–130 (2015). https://doi.org/10.1016/j.jpowsour.2015.06.144

13. K. Xu, L. Ma, X. Shen, Z. Ji, A. Yuan, L. Kong, G. Zhu, J. Zhu, Bimetallic metal-organic framework derived Sn-based nanocomposites for high-performance lithium storage. Electrochim. Acta **323**, 134855–1–134855–10 (2019). https://doi.org/10.1016/j.electacta.2019.134855.

14. H.-J. Oh, V.-D. Dao, K.-H. Ryu, J.-H. Lee, H.-S. Choi, FeSn alloy/graphene as an electrocatalyst for the counter electrode of highly efficient liquid-junction photovoltaic devices. J. Alloys Compd. **754**, 139–146 (2018). https://doi.org/10.1016/j.jallcom.2018.04.227

15. M. Poate, K.N. Tu, J.W. Meyer (eds.), *Thin Films-Interdiffusion and Reaction* (Willey-Interscianse, New York, 1978)

16. K.N. Tu, J.W. Mayer, L.C. Feldman, *Electronic Thin Film Science for Electrical Engineers and Materials Scientists* (Macmillan, New York, 1992)

17. J.E.G. Colgan, A review of thin-film alumitide formation. Mater. Sci. Rep. **5**, 1–44 (1990). https://doi.org/10.1016/S0920-2307(05)80005-2

18. R. Pretorius, C.C. Theron, A. Vantomme, J.W. Mayer, Compound phase formation in thin film structures. Crit. Rev. Solid State Mater. Sci. **24**, 1–62 (1999). https://doi.org/10.1080/10408439991329161

19. T. Laurila, J. Molarius, Reactive phase formation in thin film metal/metal and metal/silicon diffusion couples. Crit. Rev. Solid State Mater. Sci. **28**, 185–230 (2003). https://doi.org/10.1080/10408430390261955

20. V.G. Myagkov, Yu.L. Mikhlin, L.E. Bykova, V.K. Mal'tsev, G.N. Bondarenko, Long-range chemical interaction in solid-state synthesis: the formation of a CuAu alloy in Au/β-Co(001)/Cu(001) epitaxial film structures. JETP Lett. **90**, 111–115 (2009). https://doi.org/10.1134/S0021364009140069.

21. V.G. Myagkov, L.E. Bykova, A.A. Matsynin, M.N. Volochaev, V.S. Zhigalov, I.A. Tambasov, Yu.L. Mikhlin, D.A. Velikanov, G.N. Bondarenko, Solid state synthesis of Mn$_5$Ge$_3$ in Ge/Ag/Mn trilayers: structural and magnetic studies. J. Solid State Chem. **246**, 379–387 (2017). https://doi.org/10.1016/j.jssc.2016.12.010

22. V.G. Myagkov, Yu.L. Mikhlin, L.E. Bykova, G.V. Bondarenko, G.N. Bondarenko, Long-range nature of chemical interaction in solid-phase reactions: formation of martensite phases of an Au-Cd Alloy in Cd/Fe/Au film systems. Doklady Phys. Chem. **431**, 52–56 (2010). https://doi.org/10.1134/S0012501610030036

23. V.G. Myagkov, V.C. Zhigalov, L.E. Bykova, G.N. Bondarenko, Long-range chemical interaction in solid-state synthesis: chemical interaction between Ni and Fe in epitaxial Ni(001)/Ag(001)/Fe(001) trilayers. Int. J. SHS, **18**, 117–124 (2009). https://doi.org/10.3103/S1061386209020095.

24. V. Myagkov, O. Bayukov, Y. Mikhlin, V. Zhigalov, L. Bykova, G. Bondarenko, Long-range chemical interactions in solid-state reactions: effect of an inert Ag interlayer on the formation of L1$_0$-FePd in epitaxial Pd(001)/Ag(001)/Fe(001) and Fe(001)/Ag(001)/Pd(001) trilayers. Philos. Mag. **94**, 2595–2622 (2014). https://doi.org/10.1080/14786435.2014.926037

25. V.G. Myagkov, A.A. I vanenko, L.E. Bykova, V.S. Zhigalov, M.N. Volochaev, D.A. Velikanov, A.A. Matsynin, G.N. Bondarenko, Solid-state synthesis, magnetic and structural properties of interfacial B2-FeRh(001) layers in Rh/Fe(001) films, Sci. Rep **10**, 10807 (2020). https://doi.org/10.1038/s41598-020-67837-2.

26. V.G. Myagkov, L.E. Bykova, V.S. Zhigalov, A.A. Matsynin, D.A. Velikanov, G.N. Bondarenko, Solid-state synthesis, rotatable magnetic anisotropy and characterization of Co$_{1-x}$Pt$_x$ phases in 50Pt/50fccCo(001) and 32Pt/68fccCo(001) thin films. J. Alloys Compds (2021). https://doi.org/10.1016/j.jallcom.2020.157938

27. T. Shinjo, N. Hosoito, S. Hine, T. Takad, Reaction at Fe-Sn interface studied by Mössbauer spectroscopy. Jpn. J. Appl. Phys. **19**, L531–L533 (1980). https://doi.org/10.1143/JJAP.19.L531

28. M. Hida, M. Kajihara, Observation on isothermal reactive diffusion between solid Fe and liquid Sn. Mater. Trans. **53**, 1240–1246 (2012). https://doi.org/10.2320/matertrans.M2012060

29. S.-J. Hsu, C.C. Lee, Growth Kinetics of Intermetallic Compounds Between Sn and Fe Liquid–Solid Reaction Couples, J. Electron. Packaging 138 (2016) 041006–1 – 041006–5, https://doi.org/10.1115/1.40348425.

30. Y.-C. Huang, S.-W. Chen, W. Gierlotka, C.-H. Chang, J.-C. Wu, Dissolution and interfacial reactions of Fe in molten Sn-Cu and Sn-Pb solders. J. Mater. Res. **22**, 2924–2929 (2007). https://doi.org/10.1557/JMR.2007.0361

31. C.-W. Hwang, K. Suganuma, J.-G. Lee, H. Mori, Interface microstructure between Fe-42Ni alloy and pure Sn. J. Mater. Res. **18**, 1202–1210 (2003). https://doi.org/10.1557/JMR.2003.0165

32. Y.-W. Yen, H.-M. Hsiao, S.-W. Lin, P.-J. Huang, C. Lee, Interfacial reactions in Sn/Fe-xNi couples. J. Electron. Mater. **41**, 144–152 (2012). https://doi.org/10.1007/s11664-011-1727-5

33. S. Moncher, G. Principi, L.M. Gratton, C. Tosello, I. Czakó-Nagy, A. Vértes, Effect of Xe ion irradiation of Fe/Sn bilayers.

Hyperfine Interact **46**, 535–540 (1989). https://doi.org/10.1007/BF02398240FeSn2

34. S. Chikazumi, Epitaxial growth and magnetic properties of single-crystal films of iron, nickel, and permalloy. J. Appl. Phys. **32**, 81S (1961). https://doi.org/10.1063/1.2000506

35. K. Sato, T. Mizoguchi, Simple analysis of torque measurement of magnetic thin films. J. Appl. Phys. **47**, 4669–4671 (1976). https://doi.org/10.1063/1.322398

36. Y. Goto, T. Yanase, T. Shimada, M. Shirai, T. Nagahama, Tunnel magnetoresistance effect in a magnetic tunnel junction with a B2-Fe_3Sn electrode. AIP Adv. **9**, 085322-1–085322-4 (2019). https://doi.org/10.1063/1.5113544.

37. T. dos Santos, C. Bormio-Nunes, L. Ghivelder, A.R. Belarmino, Magnetostriction of Fe–Sn polycrystalline alloys. J. Magn. Magn. Mater. **320**, e183–e185. https://doi.org/10.1016/j.jmmm.2008.02.043.

38. C.V. Thompson, Solid-state dewetting of thin films. Annu. Rev. Mater. Res. **42**, 399–434 (2012). https://doi.org/10.1146/annurev-matsci-070511–155048

39. F. Leroy, Ł Borowik, F. Cheynis, Y. Almadori, S. Curiotto, M. Trautmann, J.C. Barbe, P. Müller, How to control solid state dewetting: a short review. Surf. Sci. Rep. **71**, 391–409 (2016). https://doi.org/10.1016/j.surfrep.2016.03.002

40. D. Gentili, G. Foschi, F. Valle, M. Cavallini, F. Biscarini, Applications of dewetting in micro and nanotechnology. Chem. Soc. Rev. **41**, 4430–4443 (2012). https://doi.org/10.1039/c2cs35040h

41. A. Herz, D. Wang, Th. Kups, P. Schaaf, Solid-state dewetting of Au/Ni bilayers: The effect of alloying on morphology evolution. J. Appl. Phys. **116**, 044307-1–044307–7 (2014). https://doi.org/10.1063/1.4891448

42. S. Kunwar, P. Pandey, S. Pandit, M. Sui, J. Lee, Tunable localized surface plasmon resonance by self-assembly of trimetallic and bimetallic alloy nanoparticles via Ag sublimation from Ag/Au/Pt trilayers. Appl. Surf. Sci. **504**, 144545 (2020). https://doi.org/10.1016/j.apsusc.2019.144545

43. T. Dietl, K. Sato, T. Fukushima, A. Bonanni, M. Jamet, A. Barski, S. Kuroda, M. Tanaka, P.N. Hai, H. Katayama-Yoshida, Spinodal nanodecomposition in semiconductors doped with transition metals. Rev. Mod. Phys. **87**, 1311–1377 (2015). https://doi.org/10.1103/revmodphys.87.1311